RESEARCH ARTICLE

Quantitative prediction of the 3D permeability tensor for a fractured reservoir in the Dingbian oilfield, Ordos basin, Central China

Jingshou Liu[1,2,3] (ID) | Li Dong[4] | Wenlong Ding[5] | Xiaofei Wu[6] | Yang Gu[7]

[1]Key Laboratory of Deep Oil and Gas, China University of Petroleum, Qingdao, China

[2]School of Geosciences, China University of Petroleum, Qingdao, China

[3]State Key Laboratory of Oil and Gas Reservoir Geology and Exploitation, Chengdu University of Technology, Chengdu, China

[4]SINOPEC Petroleum Exploration and Production Research Institute, Beijing, China

[5]School of Energy Resources, China University of Geosciences, Beijing, China

[6]School of Mechanics and Engineering, Southwest Jiaotong University, Chengdu, China

[7]Geoscience Documentation Center, CGS, Beijing, China

Correspondence
Jingshou Liu, School of Geosciences, China University of Petroleum, Qingdao 266580, China.
Email: liujingshou@126.com

Abstract

Understanding existing fractures is critical to achieving high and stable yields in low-permeability reservoirs, tight sandstones, and shale reservoirs. When multiple fracture sets are present in a reservoir, accurately determining the seepage direction of fluids is critical for the deployment of the well network, fracture reformation, and the design of horizontal wells. In this paper, based on conventional logging data calculations and rock triaxial mechanical experiments, a heterogeneous finite element model was established using the finite element software. The densities and the occurrence of the natural fractures were calculated by numerical simulation of the paleostress field; the fracture apertures were calculated numerically by a current in situ stress simulation. Using a combined static coordinate system and dynamic coordinate system approach, a model suitable for determining the 3D permeability tensor of multiple fractures is established, and the formula of the permeability tensor is given. In addition, by adjusting the rotation angle and flip angle in the dynamic coordinate system, the permeability of elements is predicted for different directions. The results show that fractures mainly trend in the NE (45°) and ESE (120°) directions. Additionally, the results of differential strain, microseismic monitoring, stress relief, and regional borehole collapse observations indicate that the dominant direction of the in situ stress field is ENE (70°). The principal values of maximum permeability in the reservoirs in the Chang 7_1 layer mainly range from 0.05 to 2×10^{-3} μm², and in the horizontal plane, the direction of maximum principal permeability ranges from 56 to 124°.

KEYWORDS

finite element method (FEM), fractured reservoir, permeability tensor, quantitative prediction, stress field simulation

www.manaraa.com

1 | INTRODUCTION

In the exploration and development process of low-permeability reservoirs, fractures are the main path for oil and gas seepage, and anisotropy in the fracture permeability is the dominant factor that affects the oil-water flow direction.[1-3] The difficulty in the exploration and development of fractured reservoirs lies in the prediction of the distribution range and the degree of development of fractures in the reservoir rocks, as well as the analysis and evaluation of fracture permeability anisotropy.[4-13] In underground reservoirs, the distribution of natural fractures is very complicated, and the fracture permeability anisotropy is affected by multiple factors such as the fracture occurrence, density, and aperture.

The formation and distribution of natural fractures are controlled by the paleotectonic stress field, and rock mechanics parameters play a critical role in the distribution of the paleostress field in the Ordos Basin.[11,14-18] The finite element method (FEM) is generally used to analyze the tectonic stress field (paleo- and current) and has been well verified. Therefore, it is important to establish a finite element model and reconstructing the stress field.[7,16,19-22] Studies of in situ stress based on well measurements are relatively common.[23,24] Through paleomagnetism experiments, anisotropic sound velocity methods, and field measurement methods, such as borehole collapse, hydraulic fracturing, and downhole microseismic methods, the magnitude and orientation of the in situ stress in a well can be determined.[21,25] In addition, many researchers have proposed in situ stress calculation models based on conventional and acoustic image logs.[26-28] However, it is difficult to accurately describe the distribution of the stress field in a reservoir using discontinuous point data collected at wells and 1D continuous data calculated based on well logs. To predict the interwell stress distribution, in situ stress field simulations based on the FEM have become a common analytical prediction technique.[15,21]

Snow[29] determined the permeability tensor of fractured rocks by statistical analysis of the distribution characteristics of directional fractures. Oda[30] proposed a statistical theory-based method to deduce the permeability tensor. Renard et al[31] and Min et al[32] adopted a numerical method of rock stretching and shear deformation to study the stress sensitivity of the fracture permeability. Wong and Du[33] and Wong and Li[34] proposed a mathematical flow model based on the stress sensitivity of fractured reservoirs and suggested that the variation in fracture permeability anisotropy is caused by stress. Bagheri and Settari,[35] Hassanpour et al[36] and Dayani et al[37] studied the permeability tensor of a fracture through numerical simulations. Metwally and Chesnokov[38] studied the permeability tensor of shale through laboratory measurements and established a relationship between the permeability anisotropy and the effective pressure. Rong et al[39] proposed a new calculation model for the permeability tensor

and established a constitutive model for the elastic fracturing of rocks, including consideration of fracture expansion during the shearing process. Chen et al[40] derived the theoretical relationship between shale permeability and effective stress and discussed the correlation between the fracture compressibility and the shale characteristics. Pereira[41] used the grayscale lattice Boltzmann (LB) method to determine the flow of two immiscible fluids through this three-dimensional porous medium.

In calculations of the fracture permeability tensor, many models have considered the complexity of natural fractures, the heterogeneity of the stress distribution, and the practical applications in geological modeling and reservoir engineering. To our knowledge, when multiple fractures (with different scales, formation timing, apertures, and densities) are present, determining the principal permeability in a fracture is difficult, especially in reservoir simulations, fracture predictions, and development engineering applications. The methods of measuring and calculating (or predicting) the permeability tensor in the published literatures are suitable for calculating only the direction of the principal stress or the magnitude of permeability in the direction of the coordinate axis. Therefore, precisely determining the direction of maximum permeability in an anisotropic medium remains a challenging issue. In traditional numerical simulations, geological modeling, and fracture modeling, the form of a vector or scalar is often adopted to characterize the permeability of fractures, but it is assumed that the geodetic coordinate axis is in the same direction as the principal permeability. If the direction of the principal permeability in the plane is considerably different from the direction of the geodetic coordinate axis, the application of a simple vector to characterize the permeability can cause relatively large errors in the subsequent quantification of the permeability anisotropy. Therefore, the establishment of a multicoordinate model can provide a more accurate method for calculating the direction of maximum permeability. In this paper, through the paleostress field and in situ stress field, the 3D distributions of fracture density, aperture, and occurrence are predicted. Based on the mathematical model of dynamic and static coordinate systems, a new quantitative prediction method of fracture permeability tensor is proposed that can accurately output the permeability of any section and direction. This method and model can be widely used in fractured reservoir simulation, fracture characterization prediction, horizontal well design, and development well pattern deployment.

2 | GEOLOGICAL SETTING

The study area, the Fanxue block, is located in Dingbian County, Shaanxi Province, and is structurally located in the western Ordos Basin, central China. The tectonic

form of the basin is generally a north-south asymmetrical rectangular basin that is open to the east and steep to the west (Figure 1A). The fractures and folds at the edge of the basin are relatively well developed, while the internal structure of the basin is simple and the stratum is flat, with a slope generally less than 1° (Figure 1A). As shown in Figure 2, the main strata that developed in the Dingbian area are the Upper Triassic Yanchang Formation, Jurassic Fuxian Formation, Yan'an Formation, Zhiluo Formation, and An'ding Formation as well as some Cretaceous and Quaternary strata. The Triassic Yanchang Formation is the main natural gas and oil formation in this area. The Upper Triassic Yanchang Formation is subdivided into 10 layers according to its oil-bearing formation. The lower Upper Triassic Yanchang Formation mainly includes deltaic facies and lacustrine facies. The source of the Chang 7 oil-bearing formation is mainly from the northeast, in the depositional environment of the delta front.[42-44] The sands of the Chang 7 oil-bearing formation are from a semideep lake turbidite fan, in which the turbidite fan is divided into slope-shifting turbidite fans and slump turbidite fans (Figure 1B). Analysis of the test data of the Chang 7 oil-bearing formation shows that the main porosity distribution ranges from 7% to 11%, and the main permeability

distribution ranges from 0.1×10^{-3} μm^2 to 1×10^{-3} μm^2, indicative of an ultralow porosity, ultralow permeability reservoir.

The Chang 7 sandstone is mainly lithic quartz sandstone, followed by feldspar lithic sandstone. The main clastic components are quartz and rock debris. According to statistics from the cores of the study area, the average quartz content is 55.7%, with feldspar and cuttings accounting for 11.4% and 23.6%, respectively. According to the distribution characteristics of the core pore throat, the radius distribution of the pore throat primarily has a single peak, the throat distribution range is narrow, and the peak value is mainly distributed between 0.1 and 1 μm, which are characteristics indicative of a fine throat and fine tunnel (Figure 3). By calculating the physical data and log interpretation data of some samples in the Fanxue area, the coefficient of variation of permeability is 2.78, the coefficient of penetration is 18.15, the permeability gradient is 96 000, and the coefficient of homogeneity of permeability is 0.055. Therefore, for the tight reservoir in the study area, because of its strong heterogeneity, the traditional homogeneous geomechanical modeling of simple facies attributes is not applicable. The heterogeneous modeling of reservoir geomechanics is the premise of fine stress field simulations and reservoir fracture predictions.
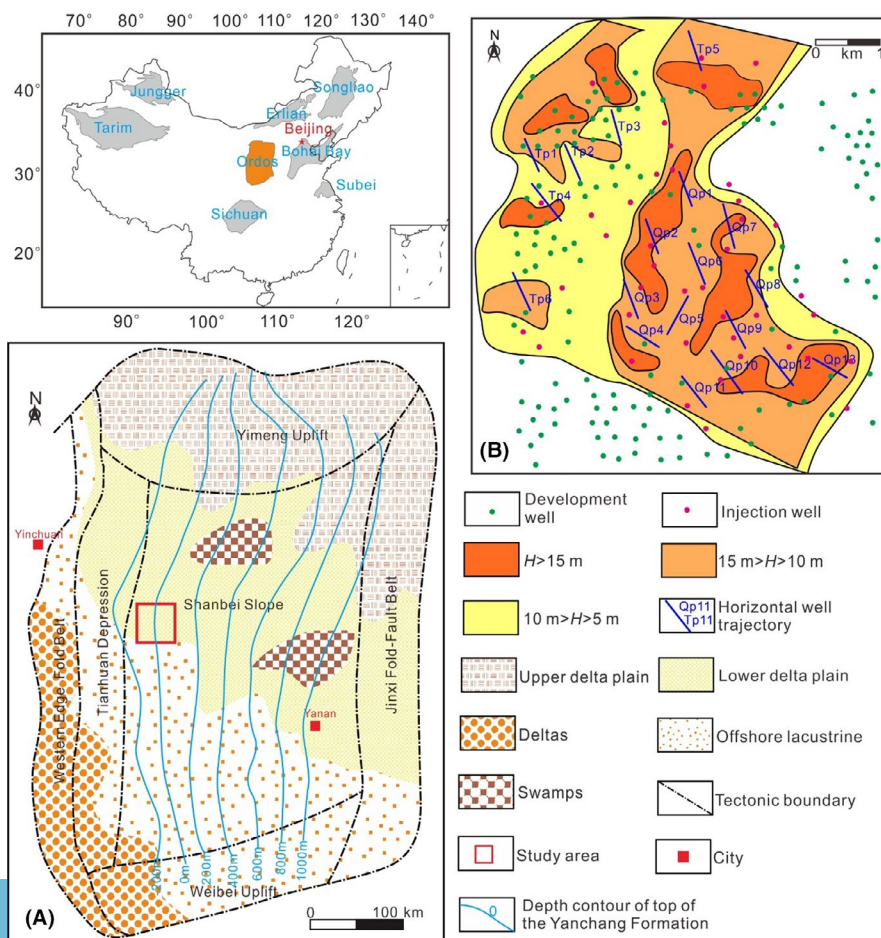
FIGURE 1 (A) Location of the Fanxue block (modified according to Zeng et al[12]); and (B) sandstone thickness distribution of the Chang 7$_1$ layer in the Fanxue block; H is the sandstone thickness
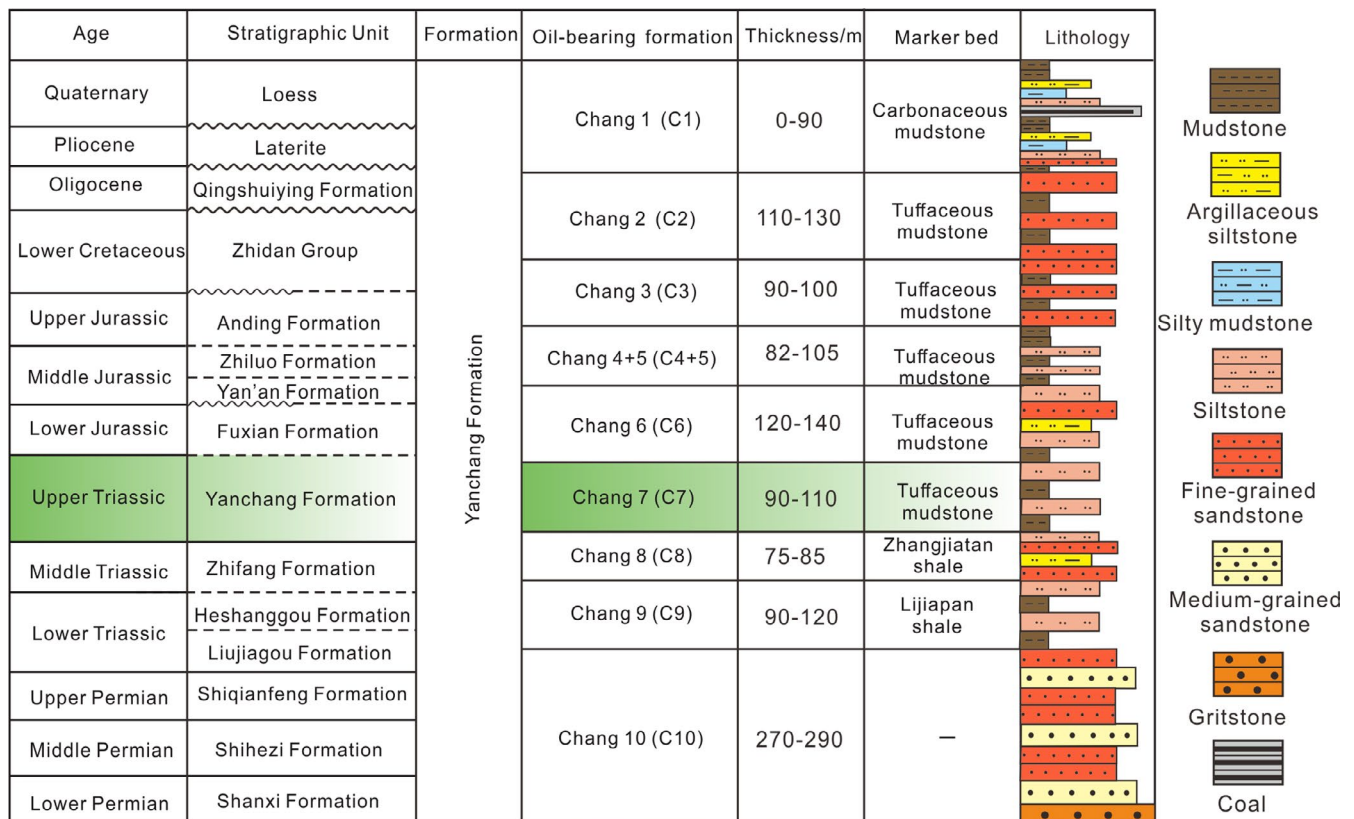
3 | THEORY AND METHODS

In this paper, using the paleostructural restoration results at different periods, a geological model for the numerical simulation of the paleo- and current stress fields is established. Through analyses of core observations, the direction of the paleostress field during the period of fracture formation is determined. According to the types of logging curves, the distance from the study area (<600 m), and the distribution of sedimentary facies, we selected 145 wells with acoustic logging and density logging for geomechanical modeling. Through triaxial mechanical experiments and conventional logging interpretation results from 145 wells, a 3D heterogeneous finite element model of the study area is established using finite element software. Based on the results of differential strain, microseismic monitoring, stress relief, and regional borehole collapse measurements, the direction of the maximum horizontal principal stress in the Fanxue block is determined. By determining the stress boundary and displacement constraints, the boundary conditions for the simulation of the paleo- and current stress fields are determined (Figure 4). Then, the occurrence and density of fractures are predicted through the proposed method of paleostress field simulation. The fracture aperture is analyzed by simulating the magnitude and direction of the maximum horizontal principal stress and the rock

mechanics parameters. Additionally, the rotation angle and flip angle are continuously transformed in the dynamic coordinate system to obtain the permeability ellipsoid data of fractures by establishing a model of the 3D fracture permeability tensor. Moreover, the planar distribution of the principal values of fracture permeability and the directions of principal values are determined (Figure 4). In general, 3D models of the fracture permeability tensor are suitable for calculating the permeability tensors of all types of fracture reservoirs and provide information for simulations of fractured reservoirs, the deployment of well networks, geological modeling, the design of horizontal wells, and fracture construction.

3.1 | Multiparameter calculation model of fractures

3.1.1 | Calculation model for subsurface fracture aperture

Although the in situ stress field is not producing new natural fractures, it affects the previously formed underground fracture system. Therefore, determining the magnitude and direction of the in situ stress field is critical for evaluating the fracture openings of unfilled fractures. Under the influence

Age	Stratigraphic Unit	Formation	Oil-bearing formation	Thickness/m	Marker bed	Lithology
Quaternary	Loess		Chang 1 (C1)	0-90	Carbonaceous mudstone	
Pliocene	Laterite					
Oligocene	Qingshuiying Formation		Chang 2 (C2)	110-130	Tuffaceous mudstone	
Lower Cretaceous	Zhidan Group		Chang 3 (C3)	90-100	Tuffaceous mudstone	
Upper Jurassic	Anding Formation	Yanchang Formation	Chang 4+5 (C4+5)	82-105	Tuffaceous mudstone	
Middle Jurassic	Zhiluo Formation / Yan'an Formation		Chang 6 (C6)	120-140	Tuffaceous mudstone	
Lower Jurassic	Fuxian Formation					
Upper Triassic	Yanchang Formation		Chang 7 (C7)	90-110	Tuffaceous mudstone	
Middle Triassic	Zhifang Formation		Chang 8 (C8)	75-85	Zhangjiatan shale	
Lower Triassic	Heshanggou Formation		Chang 9 (C9)	90-120	Lijiapan shale	
	Liujiagou Formation					
Upper Permian	Shiqianfeng Formation		Chang 10 (C10)	270-290	—	
Middle Permian	Shihezi Formation					
Lower Permian	Shanxi Formation					

Mudstone

Argillaceous siltstone

Silty mudstone

Siltstone

Fine-grained sandstone

Medium-grained sandstone

Gritstone

Coal

FIGURE 2 Classification and correlation of the Yanchang Formation and its oil-bearing formation components in the western-central Ordos Basin
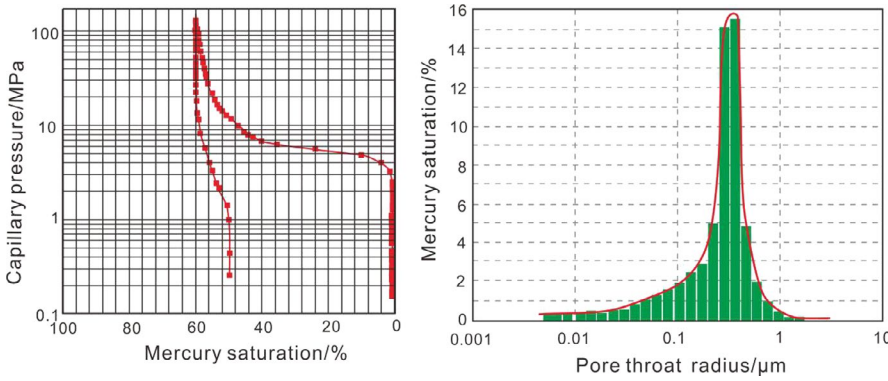
FIGURE 3 (A) Characteristics of the capillary pressure curve in the Chang 7 oil-bearing formation of the Fanxue block; and (B) pore throat probability distribution of the Chang 7 oil-bearing formation of the Fanxue block

effect of present 3D extrusion stress, the aperture can significantly decrease and cause a decline in the associated seepage. The magnitude of the fracture aperture (b) is controlled by stress and strain. If we do not consider the chemical reactions of fluids inside the fracture wall, a relatively good functional relationship exists between the stress and strain and fracture aperture b. Willis-Richards et al[45] and Hicks et al[46] proposed the following fracture aperture model:

$$b = \frac{b_0}{1 + 9\sigma'_n / \sigma_{nref}} + b_{res} \quad (1)$$

In Equation (1), b is the actual present underground fracture aperture, m; b_0 is the original fracture aperture, m; in this paper, b_0 is determined by core observation. σ'_n is the effective normal stress, MPa; and b_{res} represents the fracture aperture when the fracture surface bears the maximum effective normal stress. Because b_{res} is very small, the value is zero in the simulation. Additionally, σ_{nref} is the effective normal stress that corresponds to a 90% reduction in the fracture aperture and the magnitude of this parameter varies with differences in the lithology. Durham and Bonner[47] proposed a high value of σ_{nref} (greater than 200 MPa). Willis-Richards et al[45] proposed that σ_{nref} was between 10 and 26 MPa. Qin[48] proposed that for rock samples with uniaxial compressive strength between 30 and 50 MPa, σ_{nref} can be set to 30 MPa. In addition, σ'_n in Equation (1) is the effective normal stress:

$$\sigma'_n = \sigma_n - p_o \quad (2)$$

In Equation (2), σ_n is the normal stress perpendicular to the fracture surface, MPa; p_o is the pore pressure, MPa.

3.1.2 | Prediction model for fracture occurrence and linear fracture density

According to the numerical simulation results of the paleostress field and the rock mechanics parameters, the occurrence of fractures can be calculated by choosing appropriate rock fracture criteria. The fracture model for rock is different

from the coordinate system of the stress field; therefore, a specific mathematical transformation model is needed to obtain the actual fracture occurrence. Therefore, we define the normal vector of the fracture surface as $\boldsymbol{n}$. The angle between the principal stress and the geodetic coordinate system is defined as follows:

1. The angle between the maximum principal stress and the three coordinate axes is expressed as α_{11}, α_{12}, and α_{13};
2. The angle between the intermediate principal stress and the three coordinate axes is expressed as α_{21}, α_{22}, and α_{23};
3. The angle between the minimum principal stress and the three coordinate axes is expressed as α_{31}, α_{32}, and α_{33}.

In finite element software, the specific algorithm for converting the stress field coordinate system into fracture occurrence is described below. $\boldsymbol{n}$ can be expressed in the stress field coordinate system as follows:

$$\begin{bmatrix} n'_x \\ n'_y \\ n'_z \end{bmatrix} = \begin{bmatrix} \sin \xi \\ 0 \\ \cos \xi \end{bmatrix} \quad (3)$$
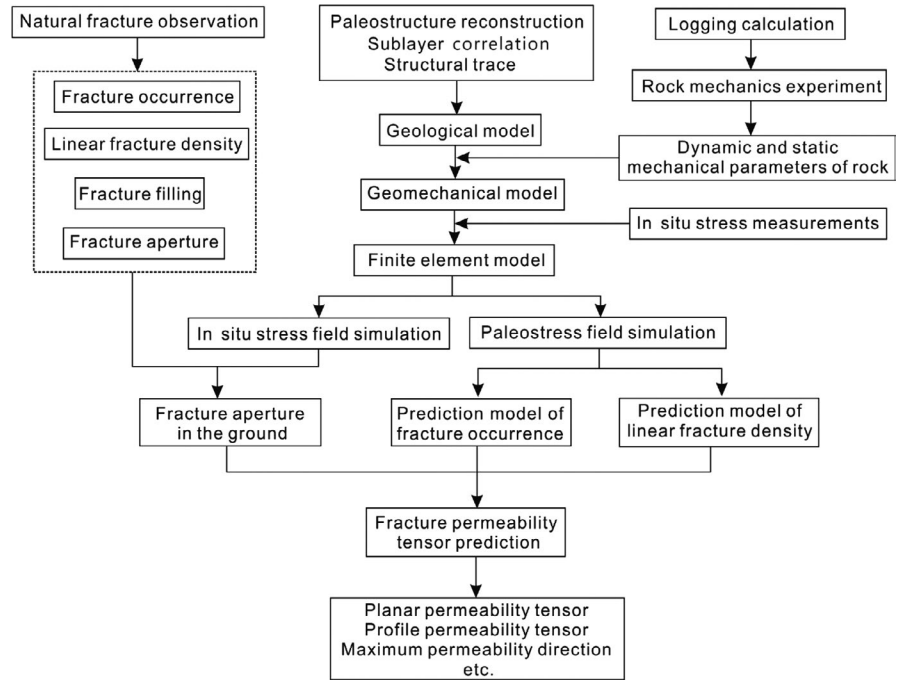
In Equation (3), ξ is the rupture angle of the rock. $\boldsymbol{n}$ can be expressed in geodetic coordinates as follows:

$$\begin{bmatrix} n_x \\ n_y \\ n_z \end{bmatrix} = \begin{bmatrix} \cos \alpha_{11} & \cos \alpha_{21} & \cos \alpha_{31} \\ \cos \alpha_{12} & \cos \alpha_{22} & \cos \alpha_{32} \\ \cos \alpha_{13} & \cos \alpha_{23} & \cos \alpha_{33} \end{bmatrix} \begin{bmatrix} n'_x \\ n'_y \\ n'_z \end{bmatrix} \quad (4)$$

According to Equation (4), the fracture dip angle (δ) and the fracture inclination (ω) can be expressed as follows:

$$\begin{cases} \tan \delta = \dfrac{\sqrt{n_x^2 + n_y^2}}{n_z} \\ \tan \omega = \dfrac{n_x}{n_y} \end{cases} \quad (5)$$

FIGURE 4 Flowchart for simulating the 3D permeability tensor of a fractured reservoir

$$\delta = \arctan\left(\frac{\sqrt{n_x^2 + n_y^2}}{n_z}\right) \tag{6}$$

$$\omega = \arctan\left(\frac{n_x}{n_y}\right) \quad (n_x \geq 0, n_y > 0) \tag{7}$$

$$\omega = \arctan\left(\frac{n_x}{n_y}\right) + \pi \quad (n_x \leq 0, n_y > 0) \tag{8}$$

$$\omega = \arctan\left(\frac{n_x}{n_y}\right) + \pi \quad (n_x < 0, n_y \leq 0) \tag{9}$$

$$\omega = \arctan\left(\frac{n_x}{n_y}\right) + 2\pi \quad (n_x \geq 0, n_y < 0) \tag{10}$$

The fracture density calculation model proposed by Liu et al[7] combined with the paleostress field simulation results allows the fracture density in different periods to be calculated.
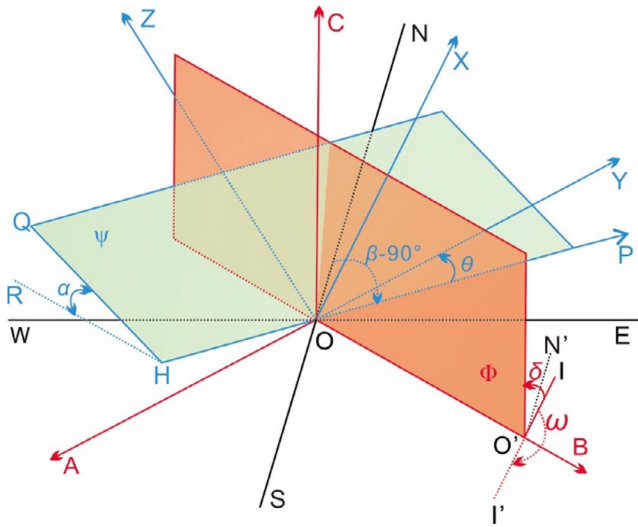
3.1.3 | 3D permeability tensor model

After underground strata break to generate fractures, the fracture permeability tensor can be studied using appropriate models. The fracture permeability anisotropy can be determined by establishing a model of the associated microelements. To satisfy the needs of this study, we assume that the element model is sufficiently small and that all the fractures can cut through it. Although previous studies established different models of fracture permeability anisotropy, the associated coordinate system was typically static. In such cases, only the permeability in the direction of the coordinate axis could be obtained, and determining the maximum permeability and minimum permeability in arbitrary directions in space is difficult. In this paper, we combine a static coordinate system and a dynamic coordinate system to reasonably solve this problem. Compared with conventional methods, a multicoordinate system has distinct advantages and solves the following issues:

1. the characterization of the permeability tensor of a complex fracture network (different apertures, densities, and occurrences);
2. the quantitative characterization of the main seepage direction and the main seepage plane in fractured reservoirs; and
3. the characterization of permeability tensors in any profile.

As shown in Figure 5, we set the dip angle of the fracture plane (Φ) as δ and the inclination as ω. I′I is the horizontal projection of the slope of Φ. The fracture is considered as a reference object to establish the coordinate system O-ABC (static coordinate system), and the three axes of coordinate system O-ABC correspond to the direction normal to the fracture plane (OA axis), the trending direction of fractures (OB axis), and the direction perpendicular to the strike of the fractures in the fracture plane (OC axis). We set the dip angle of any seepage plane ψ as α (flip angle) and the inclination as β, and the unit normal vector is $\boldsymbol{m}$. The seepage plane ψ is used as a reference to establish another coordinate system, O-XYZ (dynamic coordinate system). The θ (rotation angle) is the angle between axis OY and axis OP in the seepage plane ψ. Specifically, the OX axis is the direction normal to the seepage plane ψ, and

FIGURE 5 Geometric calculation model of the 3D fracture permeability tensor. EW is the east-west direction; S-N is the north-south direction; O-XYZ is the dynamic coordinate system; O-ABC is the static coordinate system; Φ is the fracture plane; ψ is any seepage plane; α is the dip angle of any seepage plane ψ, namely the flip angle; θ is the rotation angle; β is the inclination dip angle of any seepage plane ψ; QH is the trend line of ψ; and RH is the projection of QH in the horizontal plane

the OY axis and OZ axis are located in the seepage plane ψ. Furthermore, OP is the line of strike of the seepage plane ψ; HQ is the slope of the seepage plane ψ, and HR is the horizontal projection of the slope of ψ. Lines OS, O′N′, I′I, ON, OE, OW, HR, OH, OP, and OB are in the horizontal plane.

Based on the known linear density and underground aperture of fractures, the parallel permeability K of a single set of fractures (or individual fracture) can be expressed as follows[8]:

$$K = \frac{b^3 D_{lf}}{12} \tag{11}$$

In Equation (11), D_{lf} is the linear density of a single set of fractures, fracture/m.

Let the permeability tensor of the ith fracture be $\boldsymbol{K}$ $\boldsymbol{K}$ can be expressed in coordinate system O-XYZ as follows:

$$\boldsymbol{K} = (X, Y, Z) \cdot \boldsymbol{K}_{XYZi} \cdot \begin{bmatrix} X \\ Y \\ Z \end{bmatrix} \tag{12}$$

Similarly, the expression of the permeability tensor $\boldsymbol{K}$ in coordinate system O-ABC can be written as

$$\boldsymbol{K} = (A, B, C) \cdot KABC \cdot \begin{bmatrix} A \\ B \\ C \end{bmatrix} \tag{13}$$

Let the permeability tensor of a fracture be $\boldsymbol{K}$ $\boldsymbol{K}$ can be expressed in coordinate system O-ABC as follows.

$$\begin{bmatrix} A \\ B \\ C \end{bmatrix} = \begin{bmatrix} a & b & c \\ b & -a & 0 \\ -ac & -bc & \sin^2 \delta \end{bmatrix} \tag{14}$$

Similarly, the expression of the permeability tensor $\boldsymbol{K}$ in coordinate system O-XYZ can be written as

$$\begin{bmatrix} X \\ Y \\ Z \end{bmatrix} = \begin{bmatrix} e & f & g \\ f\cos\theta - eg\sin\theta & -fg\sin\theta - e\cos\theta & \sin^2\alpha\sin\theta \\ -eg\cos\theta - f\sin\theta & e\sin\theta - fg\cos\theta & \sin^2\alpha\cos\theta \end{bmatrix} \tag{15}$$

In coordinate system O-XYZ, the permeability tensor $\boldsymbol{K}_{ABC}$ of a single set of fractures in each element can be expressed as follows:

$$\boldsymbol{K}_{ABC} = \begin{bmatrix} 0 & 0 & 0 \\ 0 & K & 0 \\ 0 & 0 & K \end{bmatrix} \tag{16}$$

From Equations (16)-(18), we obtain

$$\boldsymbol{K}_{XYZi} = T \cdot \boldsymbol{K}_{ABC} \cdot T^T \tag{17}$$

The rotational matrix required to shift from coordinate system O-ABC to coordinate system O-XYZ is T, and it can be expressed as follows:

$$T = \begin{bmatrix} m_{11} & m_{12} & m_{13} \\ m_{21} & m_{22} & m_{23} \\ m_{31} & m_{32} & m_{33} \end{bmatrix} \tag{18}$$

In coordinate system O-XYZ, the permeability tensor $\boldsymbol{K}_{XYZi}$ of a single set of fractures (or single fracture) in the element can be expressed as follows:

$$K_{XYZi} = K \begin{bmatrix} m_{12}^2 + m_{13}^2 & m_{12}m_{22} + m_{13}m_{23} & m_{12}m_{32} + m_{13}m_{33} \\ m_{12}m_{22} + m_{13}m_{23} & m_{22}^2 + m_{23}^2 & m_{22}m_{32} + m_{23}m_{33} \\ m_{12}m_{32} + m_{13}m_{33} & m_{22}m_{32} + m_{23}m_{33} & m_{32}^2 + m_{33}^2 \end{bmatrix} \tag{19}$$

The mathematical explanations of $a, b, c, d, e, f, m_{11}, m_{12}, m_{13}, m_{21}, m_{22}, m_{23}, m_{31}, m_{32},$ and m_{33} can be found in the Appendix 1.

Under complicated geological conditions, a reservoir undergoes multiple episodes of tectonic stress field evolution and develops multiple sets of fractures, and the occurrence, density, and aperture of each fracture set are often different. According to Equations (17)-(19), when multiple fractures develop in an element, the permeability tensor K_{XYZ} can be expressed by

$$K_{XYZ} = \sum_{i=1}^{k} K_{XYZi} T_i \qquad (20)$$

In Equation (20), k is the number of fracture sets inside the element; and T_i is the rotational matrix when the ith set of fractures is transformed from the components of the O-ABC coordinate axis to the components of the O-XYZ coordinate axis.

4 | RESULTS AND DISCUSSION

4.1 | Fracture developmental characteristics

Whole core and field observations can be used to determine the mechanical features of fractures by observing the features of the fracture surface, such as forms, scratches, extension distance, roughness, and presence of gravel and fill (Figure 6A-C). Core observations indicate that the core mainly develops shear fractures, slip fractures, and overpressure fractures (Figure 6B,C). The lithology is dominated by siltstone and fine sandstone, and most of it is not filled. The observation of microfractures shows that the fractures in the study area are mostly filled with black matter, which may be organic matter, indicating that these microfractures can be used as important oil-gas migration channels and reservoir spaces (Figure 6D). The longitudinal extension length of the fractures is between 0.05 m and 1.0 m, with most less than 0.3 m, which indicates that the fractures generally develop in a single sand body. The fracture trends are mainly in the NE (45°) and ESE (120°) directions (Figure 7A). The fracture apertures of thin slices are concentrated in the range of 10-300 μm (Figure 7B), and the average fracture aperture is 130 μm.

4.2 | Stress field simulation

4.2.1 | In situ stress measurements

The use of hydraulic fractures (HFs) technology for microseismic monitoring is an effective method of directly measuring the direction of the maximum horizontal principal stress. As shown in Table 1, the results of hydraulic fracturing in the Fanxue block show that the principal stress is predominantly in the ENE (73.6°) direction. Elliptical borehole breakouts are commonly utilized to determine the orientation of the in situ stress in deep sedimentary basins. The long axes of borehole breakouts are generally perpendicular to σ_H.[21-22,49-52] As shown in Table 1, the results of the borehole breakout in the Fanxue block show that the principal stress is predominantly in the ENE (62.1°) direction. As shown in Table 1, the direction of the in situ stress field in the Fanxue block is predominantly in the ENE direction, based on differential strain, microseismic monitoring, regional borehole collapse measurements, and stress relief.

The in situ stress is mainly determined by the MTS286 rock test system through acoustic emission experiments. This system is one of the most advanced acoustic emission processing systems in the world. According to the Kaiser effect principle, the acoustic emission signal at the sudden and obvious increase is found on the acoustic emission signal graph, and the magnitude of the load is recorded, which is the ground stress of the rock in the direction underground. The rock is subjected to 3D stress in the ground; thus, it is necessary to test in different directions to determine the magnitude of the principal stress in three directions. Generally, three rock samples are drilled in a direction perpendicular to the axis of the drilling core in an increment of 45°, and a vertical rock sample is taken in parallel with the core axis to obtain the Kaiser point stress in four directions. The in situ stress of the deep rock can be determined by the following equation[53]:

$$\sigma_v = \sigma_\perp + \alpha_e p_o \qquad (21)$$

$$\sigma_H = \frac{\sigma_0 + \sigma_{90}}{2} + \frac{\sigma_0 - \sigma_{90}}{2}(1 + \tan^2 2\kappa)^{\frac{1}{2}} + \alpha_e p_o \qquad (22)$$

$$\sigma_h = \frac{\sigma_0 + \sigma_{90}}{2} - \frac{\sigma_0 - \sigma_{90}}{2}(1 + \tan^2 2\kappa)^{\frac{1}{2}} + \alpha_e p_o \qquad (23)$$

$$\tan 2\kappa = \frac{\sigma_0 + \sigma_{90} - 2\sigma_{45}}{\sigma_0 + \sigma_{90}} \qquad (24)$$

In Equations (21)-(24), σ_v is the overlying formation stress; σ_H and σ_h are the maximum and minimum horizontal principal stresses, respectively; and p_o is the pore pressure. α_e is the effective stress coefficient; $\sigma_\perp$ is the core Kaiser point stress[54] in the vertical direction; and σ_0, σ_{45}, and σ_{90} are the Kaiser point stresses of three horizontal directions (0°, 45°, and 90°, respectively). Through testing five rock samples in the study area, the vertical stress gradient is 2.28 MPa/100 m, the maximum horizontal principal stress gradient is 1.96 MPa/100 m, the minimum horizontal principal stress gradient is 1.77 MPa/100 m, the minimum horizontal principal stress is 42.0 MPa, and the maximum horizontal principal stress is 46.7 MPa.

FIGURE 6 Characteristics of natural fractures observed in field and drill whole cores of the Chang 7 oil-bearing formation in the study area. (A) Conjugated vertical unsealed fractures observed in the field, where the fracture surface is straight; (B) vertical unsealed fractures with a long cutting depth in the F6403 well, 2405.12 m; and (C) small normal faults characterized by strike-slip, convergence at one end and divergence at the other, F1387 well, 2369.24 m; (D) microfractures are filled with black material
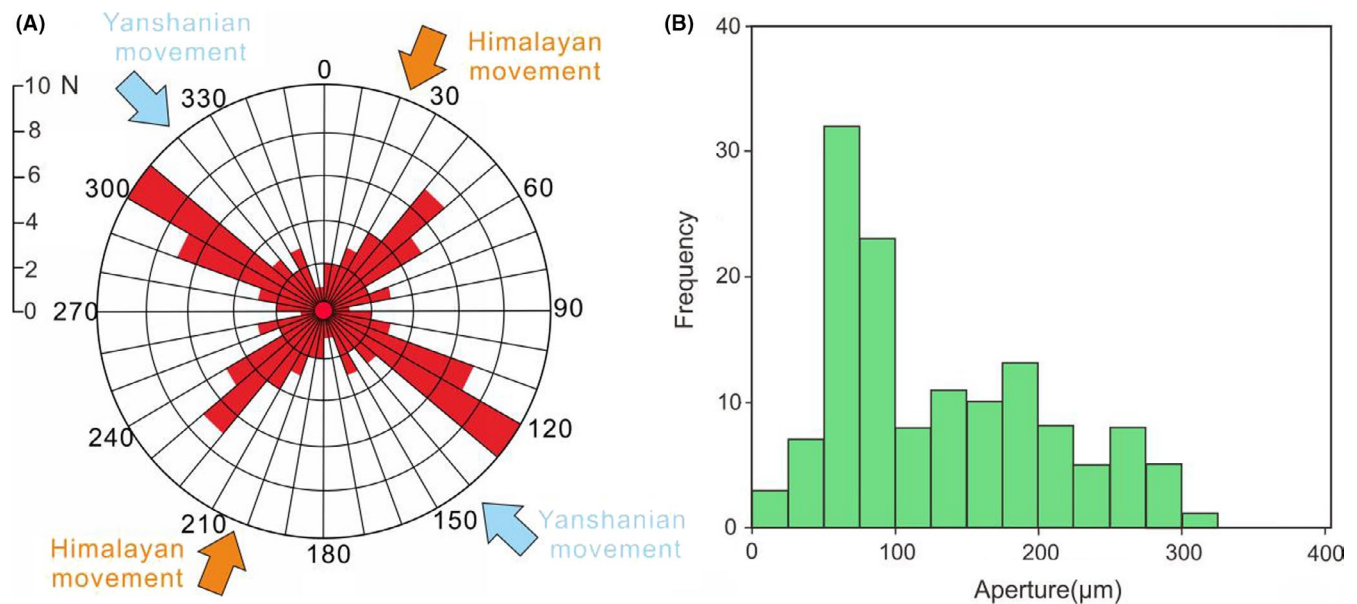
FIGURE 7 (A) Strikes of tectonic fractures, where the dominant strikes of fractures in the Fanxue block are EN-WS and ESE-WNW; and (B) frequency distribution of fracture apertures in thin slices

4.2.2 | Geological model

The distribution of the in situ stress is affected by multiple factors, such as the rock mechanical parameters and tectonic relief. In this paper, the FEM is used to simulate the 3D in situ stress field. The in situ stress field simulations include establishing geological models, mechanical models, and finite element models (mathematical models).

The geological model is established after sublayer correlation and interpolating layered data. The mechanical model is mainly based on the mechanical parameters of different lithologies determined by triaxial mechanical experiments and logging calculation. The layer model established in petrel is imported into the finite element software, and the three-dimensional finite element mesh is obtained by the method of free mesh generation. The finite element model

TABLE 1 Comparison of maximum horizontal principal compression stress from the different measurement methods in the Fanxue block

Data	Number	Quality	Direction of S_H	Region
Borehole breakouts	19	A	ENE62.13°	Regional
Differential strain	8	A	ENE66.73°	Regional
Hydraulic fractures	5	A	ENE73.60°	Local
Stress relief	1	C	ENE72°	Regional

Note: The quality ranking system of the WSM project[51] was used to assess the reliability of the results in each location.
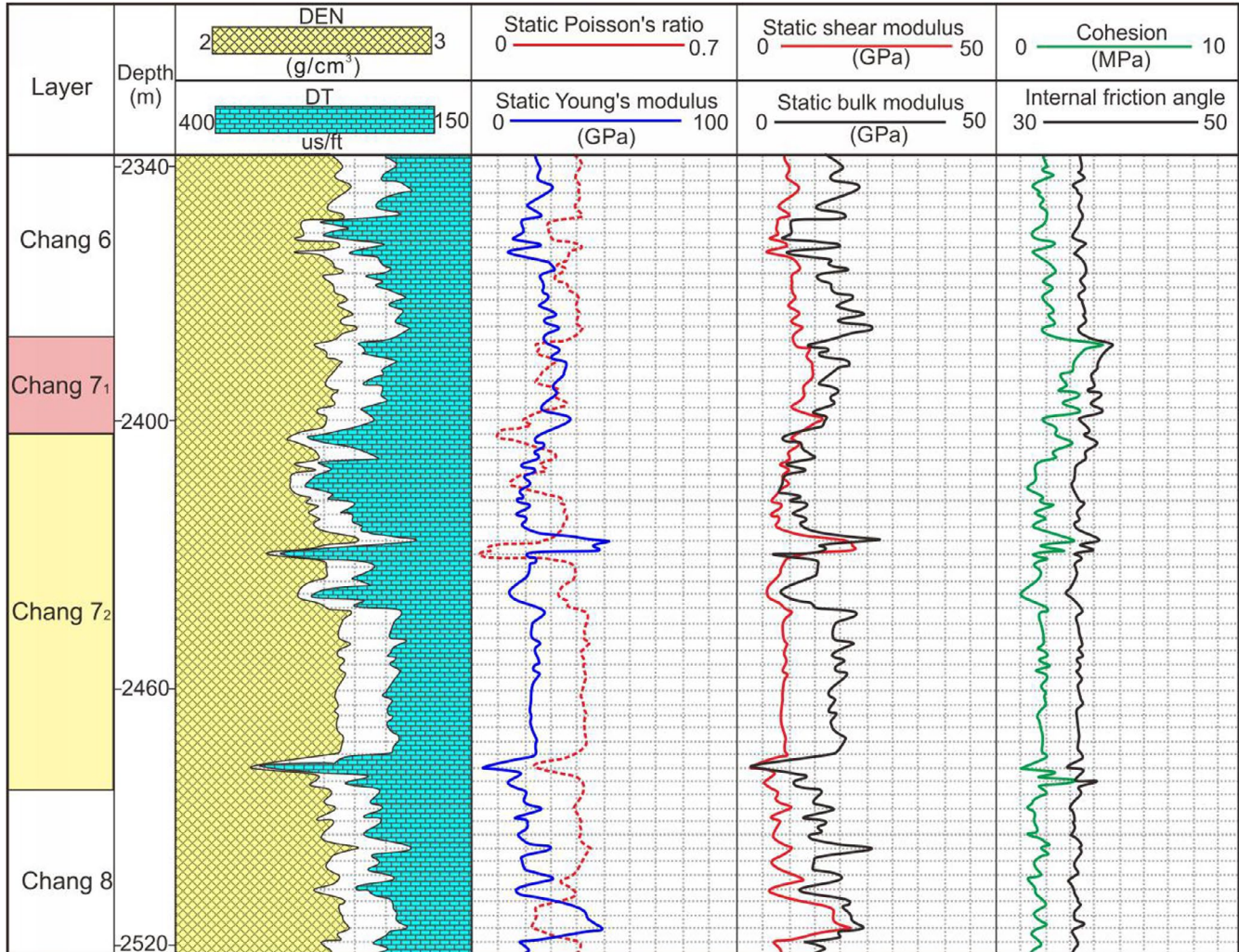
FIGURE 8 Logging interpretation results of rock mechanical parameters from the F4648 well

includes boundary conditions (stress size, stress direction, and displacement constraints) and finite element meshing. In the finite element simulation, as the required accuracy of the simulation results of the geological model increase, more calculations are needed. In this study, the target horizon is retained as a 3D heterogeneous geological structure, and other horizons are considered as a set of homogeneous formations (surrounding rocks). The geological model of the study area was established using the bottom structural map of the Chang 7₁ layer, which has an average thickness of 25 m.

4.2.3 | Mechanical model

The mechanical properties of rocks include the deformation and strength characteristics of rocks. The mechanical property parameters reflecting rock deformation characteristics are also called elastic parameters, including Young's modulus (E), bulk modulus (K_b), shear modulus (G), and Poisson's ratio (μ). The relevant formulas are as follows[55,56]:

$$E = \frac{\rho}{\Delta t_s^2} \times \frac{3\Delta t_s^2 - 4\Delta t_p^2}{\Delta t_s^2 - \Delta t_p^2} \times 10^6 \tag{25}$$

$$\mu = \frac{\Delta t_s^2 - 2\Delta t_p^2}{2\Delta t_s^2 - \Delta t_p^2} \quad (26)$$

$$G = \frac{\rho}{\Delta t_s^2} \times 9.29 \times 10^7 \quad (27)$$

$$K_b = \rho \times \frac{3\Delta t_s^2 - 4\Delta t_p^2}{3\Delta t_s^2 \Delta t_p^2} \times 9.29 \times 10^7 \quad (28)$$

Through mechanical experiments on rock samples from the Chang 7 oil-bearing formation, we determined the calculation model of internal friction angle and shear strength of rock in the study area:

$$\nu = -109.89 + 2.024E - 31.814\mu + 51\rho \quad (29)$$

$$\sigma_s = 103.553 + 1.290E - 359.85\mu + 2.0\rho \quad (30)$$

In Equations (25)-(30), ρ is the density, g/cm^3; Δt_s and Δt_p are the shear wave slowness and compressional wave slowness, respectively, μs/m; ν is the internal friction angle of the rock, °; and σ_s is the shear strength of the rock, MPa.

Based on the data of 145 development wells (19 horizontal wells) in the study area (Figure 1B), the mechanical parameters of each well are calculated, and the 3D distribution of rock attribute parameters in the study area is obtained by Kriging interpolation algorithm. Young's modulus of the rock is between 17 and 34 GPa, Poisson's ratio is between 0.18 and 0.34, and the shear strength is between 13 and 46 MPa. The density of the rock in the study area is between 2360 and 2600 kg/m^3, and the internal friction angle of the rock is between 42 and 66° (Figure 8). The static mechanical parameters of rock are obtained from the dynamic and static mechanical parameters transformation mathematical model (Figure 9D). We adopt the FEM to establish the current geomechanical model of the study area and use finite element software for numerical simulations of the in situ stress field for the Chang 7$_1$ layer in the Fanxue block.

4.2.4 | Finite element model

Previous studies have shown that the structural fractures in the western Ordos Basin were mainly formed in the Yanshanian and Himalayan periods (Figure 7A). At the end of the Jurassic, under the NWW-SEE horizontal tectonic compressive stress, the nearly EW and NW-SEE conjugate shear fractures formed. During the Late Cretaceous-Paleogene period, under the NNE-SW horizontal compressive stress field, the N-S and NE-SW conjugate shear fractures formed. However, due to the strong heterogeneity of the rock strata caused by sedimentation and diagenesis, the development degree of the two sets of conjugate shear fractures in the same period is different in different sedimentary systems. One set of fractures is restrained, and the development degree is poor. Therefore, a set of single shear fractures mainly developed in each construction period. Under the two-stage tectonic movement, the two sets are mainly composed of two orthogonal fracture systems. Through an analysis of single well burial history, it is determined that the burial depth of the Chang 7$_1$ layer in the Yanshanian period is approximately 2320 m, whereas that of the Chang 7$_1$ layer in Himalayan period is approximately 2090 m. Combined with triaxial mechanical experiment and fracture occurrence, the maximum horizontal principal stress of the Yanshanian period is 141°, and the maximum principal stress of the Himalayan period is 27°. According to Ju et al,[16] Zhao and Hou,[18] Zhao et al[57] and the fracture conditions of the rocks, it is determined that the maximum horizontal principal stress in the Yanshanian period is 145 MPa, the minimum horizontal principal stress in the Yanshanian period is 43 MPa, the maximum horizontal principal stress in the Himalayan period is 95 MPa, and the minimum horizontal principal stress in the Himalayan period is 34 MPa.
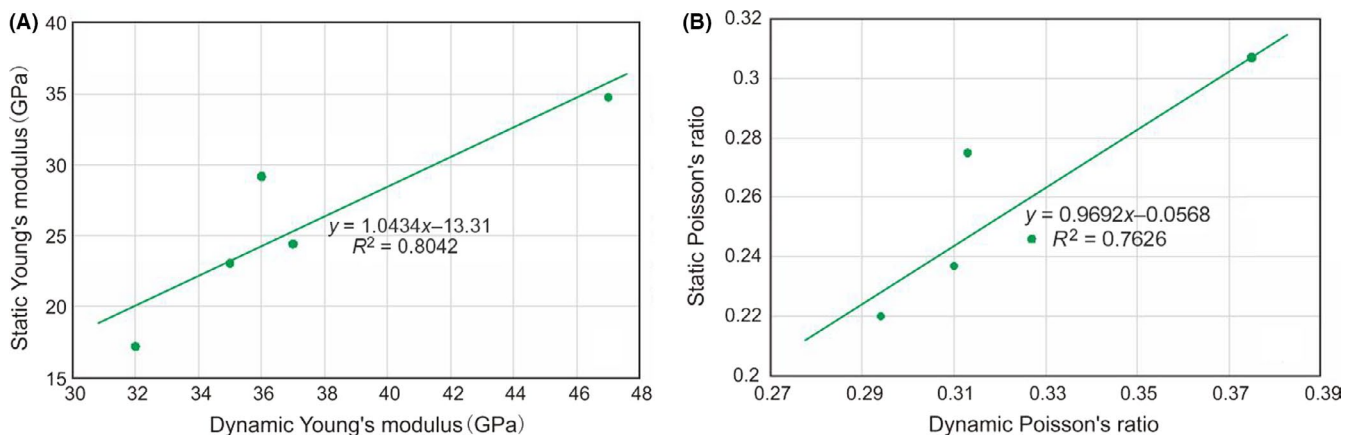
FIGURE 9 (A) Relationship between the dynamic Young's modulus and the static Young's modulus of the rock; and (B) relationship between the dynamic Poisson's ratio and the static Poisson's ratio of the rock

We adopt SOLID45 units and a relatively tight grid division for the Chang 7_1 layer; SOILD45 units are suitable for numerical simulations of 3D layered structures. The target horizon is divided into fine grids, and the average edge length of the element is set to 28 m. The surrounding rocks of the Chang 7_1 layer are partitioned with a sparse mesh. The number of elements and nodes in finite element models for different periods is shown in Table 2. Through computer programming, the calculated 3D rock mechanical parameter distribution (Figure 10) is assigned to the corresponding element. The stress boundary conditions for different periods are shown in Figure 11, and a displacement constraint in the Z direction is applied to the bottom of the model to prevent the model from moving. (Figure 11).

4.2.5 | Simulation results

In this paper, positive values represent compressive stress. The distribution characteristics of the principal stress that occurs in different periods are similar. Taking the present stress field as an example (Figure 12), the minimum principal stress is between 34 and 52 MPa, with a direction of NWW (340°), and the intermediate principal stress is between 38 and 27 MPa, with a direction of ENE (70°). The direction of the horizontal principal stress is changed by 10-20° in different positions. The maximum principal stress is in the vertical direction, which is mainly controlled by the rock density and

burial depth, and its magnitude is between 59 and 63 MPa. By using the distributions of stress, strain, and rock mechanics parameters, the fracture parameters in different units are simulated, and the permeability tensor in each unit is calculated by programming.

4.3 | Multiparameter prediction of fractures

4.3.1 | Prediction of the linear fracture density

The distribution of linear fracture density can be obtained by using the simulation results of the paleostress field and the mathematical model proposed by Liu et al.[21] As shown in Figure 13, the linear fracture density in the Himalayan period is concentrated in the range of 0.1-0.6 fractures/m, and the linear fracture density in the Yanshanian period is concentrated in the range of 0.1-1.1 fractures/m. In the Himalayan period, the fracture linear density is high in the northwest region and low in the southeast region, and the fracture is not developed. The linear fracture density in the Yanshanian period is high in the east and low in the west.

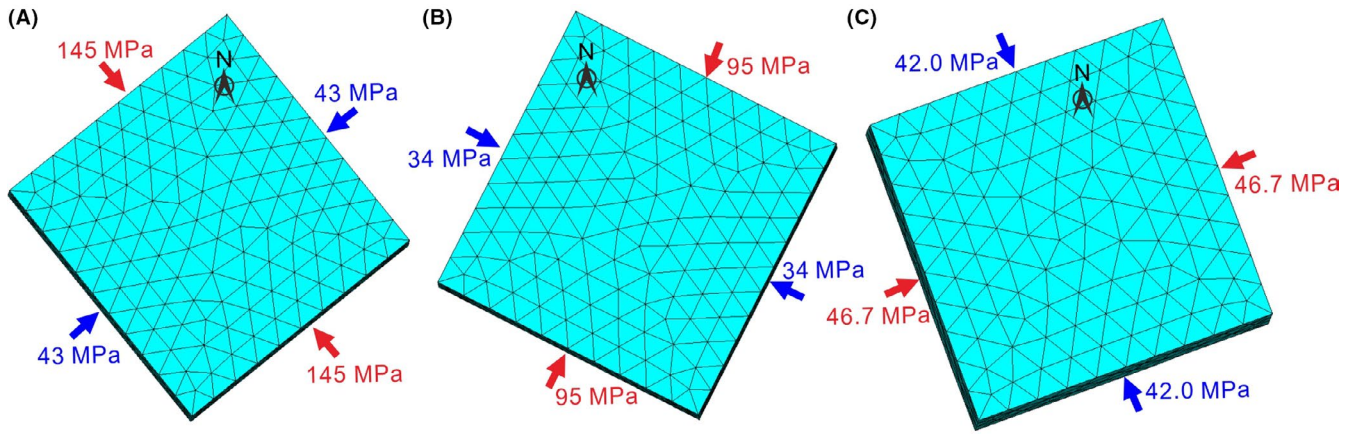### 4.3.2 | Prediction of the fracture occurrence

Through the paleostress field simulations, the distributions of two sets of fractures are determined using Equations (3)-(10). The simulated dip angle of the fracture is mainly vertical, with a dip angle of more than 80°. The simulated Himalayan fracture strikes are concentrated between 41 and 64°, and the simulated Yanshanian fracture strikes are concentrated between 111 and 131° (Figure 14). These results are consistent with those based on core observations (Figure 7A).

TABLE 2 Number of elements and nodes in finite element models in different periods in the Fanxue block

Model	Number of elements	Number of nodes
Yanshanian period	780 165	183 075
Himalayan period	790 896	184 636
Present	910 755	204 429
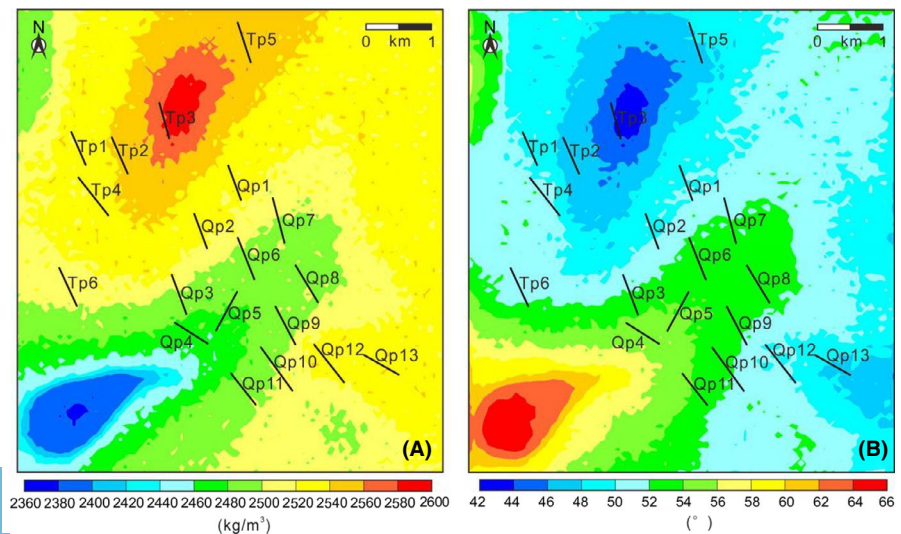
FIGURE 10 (A) Distribution of the rock density in the Chang 7_1 layer in the Fanxue block; and (B) distribution of the internal friction angle in the Chang 7_1 layer in the Fanxue block

2360 2380 2400 2420 2440 2460 2480 2500 2520 2540 2560 2580 2600
(kg/m³)

42 44 46 48 50 52 54 56 58 60 62 64 66
(°)

FIGURE 11 Mechanical model and boundary conditions for the in situ stress simulation in the Fanxue block: (A) Yanshanian model; (B) Himalayan model; and (C) current model
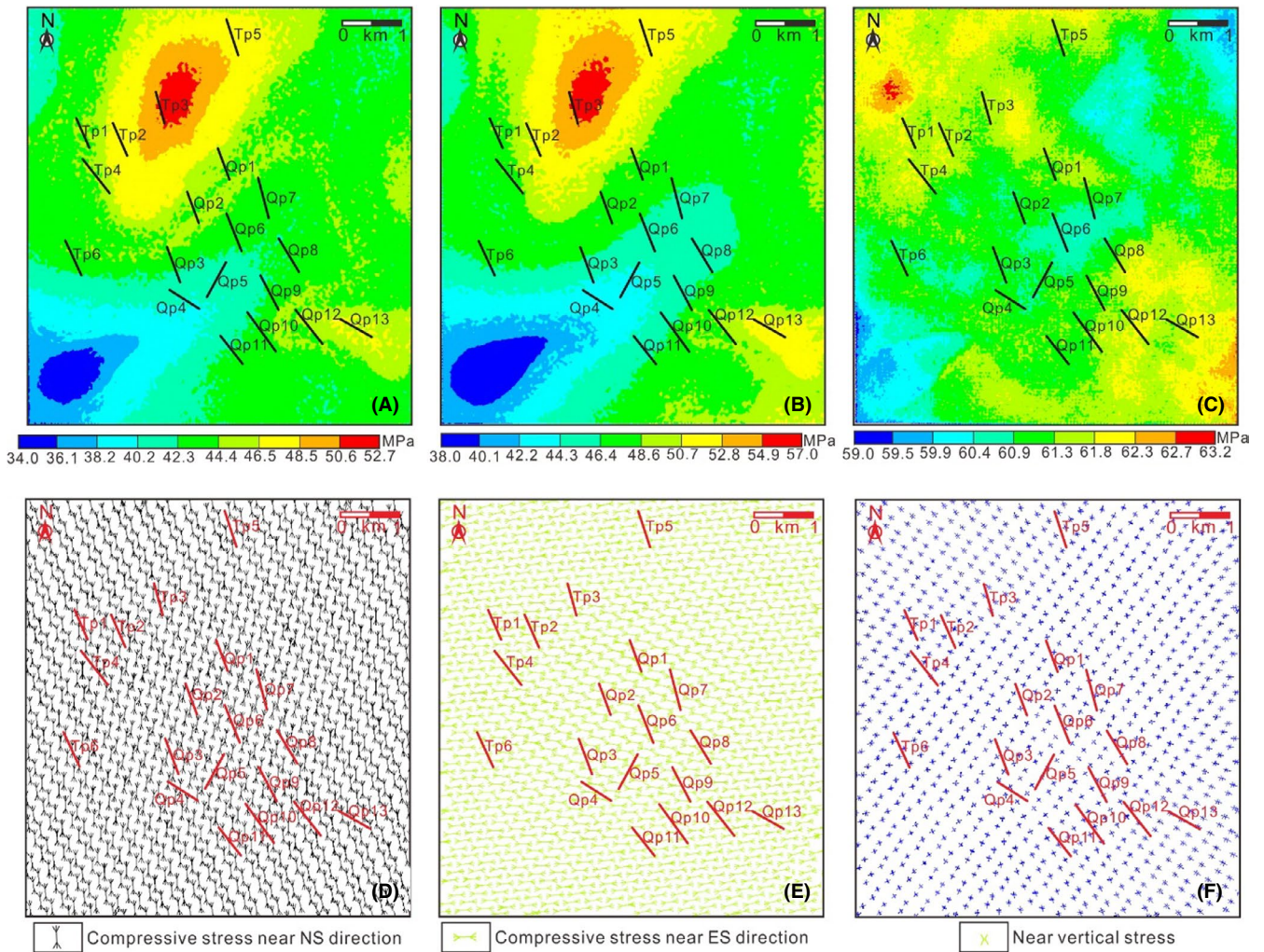

FIGURE 12 (A) Distribution of the minimum principal stress in the Fanxue block; (B) distribution of the intermediate principal stress in the Fanxue block; (C) distribution of the maximum principal stress in the Fanxue block; (D) direction of the minimum principal stress in the Fanxue block; (E) direction of the intermediate principal stress in the Fanxue block; and (F) direction of the maximum principal stress in the Fanxue block

FIGURE 13 Distribution of the linear fracture density in the study area: (A) fracture formed in the Himalayan period; and (B) fracture formed in the Yanshanian period
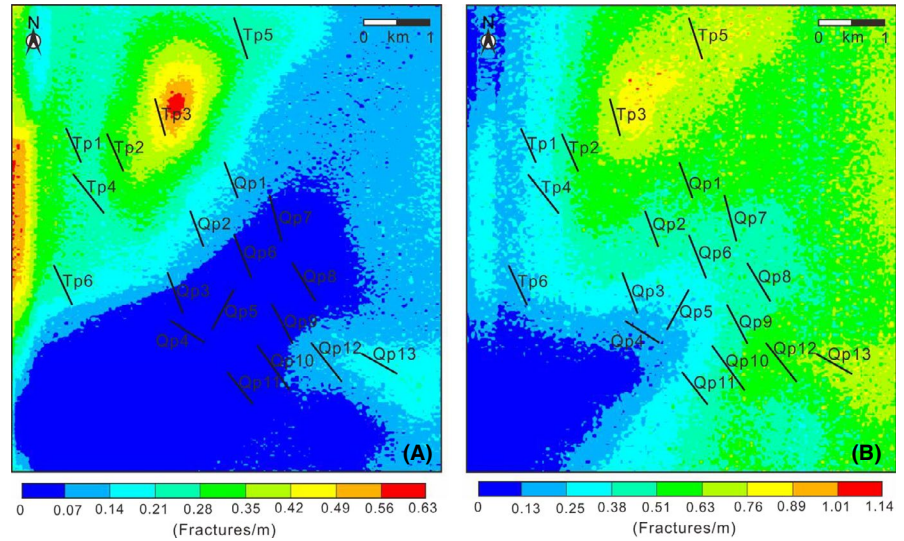
FIGURE 14 (A) Fracture strike distribution in the Himalayan period; and (B) fracture strike distribution in the Yanshanian Period
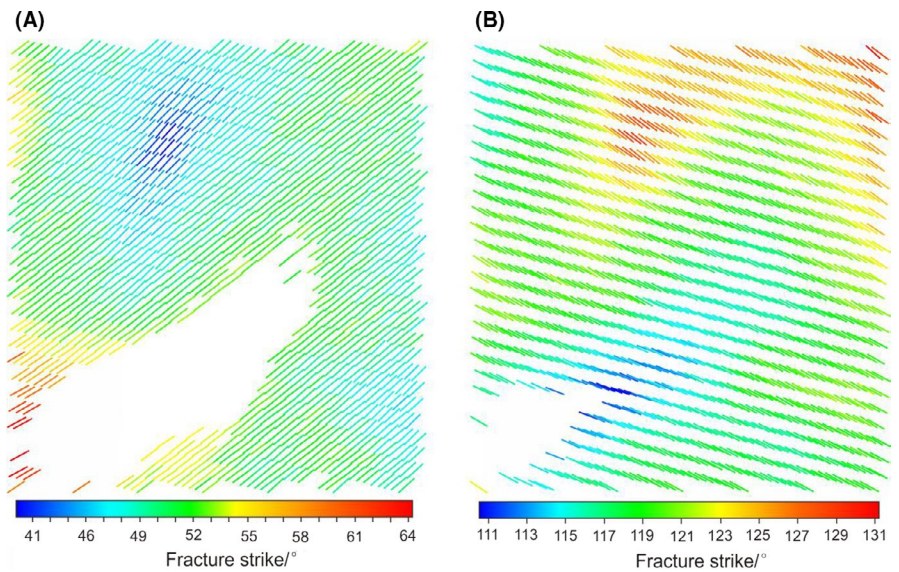

4.3.3 | Prediction of the fracture aperture

Using the results of the paleostress field simulation and Equations (1) and (2), an original fracture aperture (b_0) of 130 μm (Figure 7B), and σ_{nref} of 35 MPa, the apertures of fractures in different periods are obtained (Figure 15). The maximum horizontal principal stress in Fanxue block is in the NEE direction; therefore, the fracture aperture of the Yanshanian period is generally smaller than that of the Himalayan period. The fracture aperture in the Himalayan period is between 9 and 43 μm, and the fracture aperture in the Yanshanian period is between 9 and 22 μm. The fracture aperture is low in the vicinity of the Tp3 well, and the fracture apertures in both periods are less than 12 μm. The fracture aperture in the Himalayan period is low in the middle and high in the periphery of the Fanxue Block. The fracture aperture of the Yanshanian period is similar to that of the Himalayan period, and the value is greater than 18 μm.

4.4 | Fracture permeability tensor prediction

The linear density, aperture, and occurrence distribution of fractures in each element can be determined by simulating the stress field. Furthermore, a permeability tensor model can be established for each element. Using Equations (28)-(30), the principal value and direction of permeability in each element are output by continuously adjusting the rotation angle and the flip angle of the dynamic coordinate system O-XYZ; that is, we calculate the flip angle α and rotation angle θ in Equations (19) and (20) via cyclic calculations and output the corresponding principal value of permeability. Additionally, we can output the direction and size of the maximum permeability. As shown in Figure 16, the fracture permeability results predicted by the stress field method indicate that the maximum principal values of permeability in the Chang 7_1 layer are concentrated and distributed in the
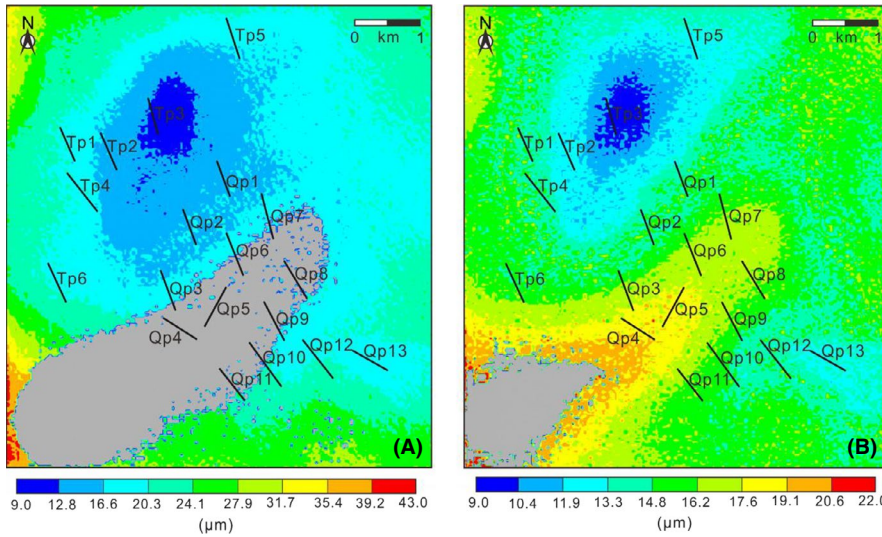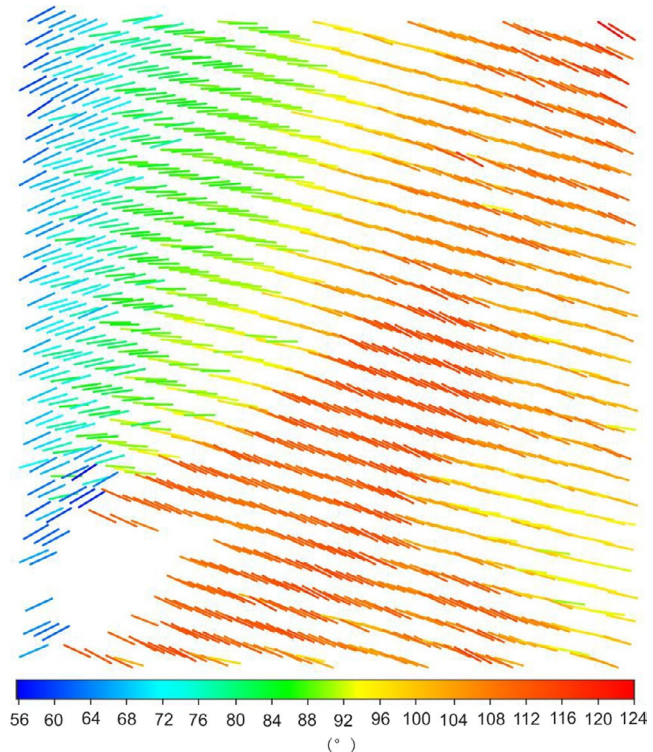
FIGURE 15 (A) Fracture distribution in the Himalayan period; and (B) fracture strike distribution in Yanshanian period. Gray represents the area where fracture does not develop
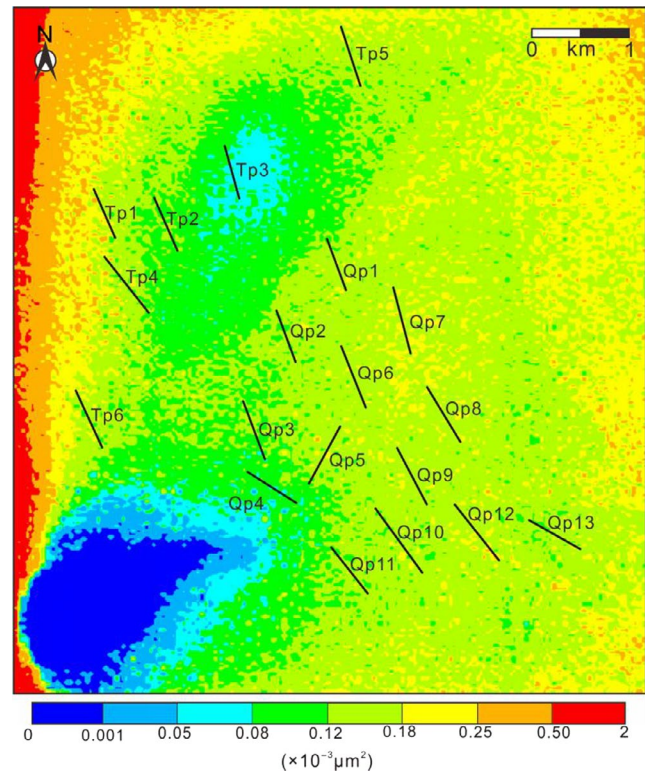
FIGURE 16 Distribution of the principal value of the fracture permeability in the study area

FIGURE 17 Distribution of the maximum horizontal permeability direction of fractures in the study area

range of 0.05-2 × 10^{-3} μm^2 (Figure 16). Specifically, in the western part of the study area, the fracture permeability is high, and the value is greater than 0.25 × 10^{-3} μm^2; in the vicinity of the Tp5 well, the principal value of fracture permeability is low, and the value is less than 0.8 × 10^{-3} μm^2. In the eastern part of the study area, the change of permeability is not significant, and the value is between 0.1 × 10^{-3} and 0.3 × 10^{-3} μm^2.

From west to east, the maximum horizontal permeability direction in the study area is generally from NEE to EW

and then to SEE. In the western margin of the study area, the maximum horizontal permeability direction is 56-72°, and in the middle and northeast of the study area, the maximum horizontal permeability direction is 100-124° (Figure 17).

5 | CONCLUSIONS

1. In this paper, we establish a quantitative prediction model using a 3D permeability tensor for multiple fractures and

give the associated formula of the permeability tensor. Based on the paleo- and current stress field numerical simulations, the fracture density, occurrence, and aperture in the element are determined. By adjusting the rotation angle and flip angle of the dynamic coordinate system, we predict the permeability of elements in different directions.

2. The aperture of the fracture formed in the Yanshanian period is generally smaller than the aperture of the fracture formed in the Himalayan period due to the influence of the maximum horizontal principal stress in NEE direction. The fracture aperture in the Himalayan period is between 9 and 43 μm, and the fracture aperture in the Yanshanian period is between 9 and 22 μm. The simulated fracture strikes in the Himalayan and Yanshanian periods are 41-64° and 111-131°, respectively. The linear fracture density is concentrated in the range of 0.1-0.6 fractures/m in the Himalayan period, and the linear fracture density is 0.1-1.1 fractures/m in the Yanshanian period. In the Himalayan period, the fracture linear density is high in the northwest region and low in the southeast region. The linear fracture density during the Yanshanian period is high in the east and low in the west. The fracture permeability results predicted by the stress field simulation show that the maximum principal permeability values in the reservoir of the Chang 7_1 layer are concentrated and distributed in the range of $0.05\text{-}2 \times 10^{-3}$ μm^2. From west to east, the maximum horizontal permeability direction in the study area is generally from ENE to EW and then ESE.

3. The permeability tensor of fractures is related to the occurrence, density, and aperture of the fractures. The occurrence and density of the fractures are predicted by recovering the paleostress field. The aperture of the fractures is determined through simulating the in situ stress. The paleostress and current stress fields can be combined to accurately calculate and predict the permeability tensors of fractured reservoirs.

ACKNOWLEDGMENTS

NOMENCLATURE

b actual present underground fracture aperture

b_0 original fracture aperture

σ'_n effective normal stress

b_{res} fracture aperture when the fracture surface bears the maximum effective normal stress

σ_{nref} effective normal stress that corresponds to a 90% reduction in the fracture aperture

σ_n normal stress perpendicular to the fracture surface

p_o pore pressure

$\boldsymbol{n}$ normal vector of the fracture surface

δ fracture dip angle

ω fracture inclination

Φ fracture plane

ψ any seepage plane

α dip angle of any seepage plane ψ

θ rotation angle

β inclination dip angle of ψ

$\boldsymbol{m}$ unit normal vector of ψ

$\boldsymbol{K}$ permeability tensor of the fracture

σ_v the overlying formation stress

σ_H maximum horizontal principal stresses

σ_h minimum horizontal principal stresses

α effective stress coefficient

$\sigma_\perp$ core Kaiser point stress in the vertical direction

ρ rock density

Δt_s shear wave slowness

Δt_p compressional wave slowness

υ internal friction angle of the rock

σ_s shear strength of the rock

E Young's modulus

K_b bulk modulus

G shear modulus

μ Poisson's ratio

ξ rupture angle of the rock

α_e effective stress coefficient

ORCID

Jingshou Liu https://orcid.org/0000-0002-5252-7555

REFERENCES

1. Laubach SE, Olson JE, Gross MR. Mechanical and fracture stratigraphy. *AAPG Bull*. 2009;93(11):1413-1426.

2. Olson JE, Laubach SE, Lander RH. Natural fracture characterization in tight gas sandstones: integrating mechanics and diagenesis. *AAPG Bull*. 2009;93(11):1535-1549.

3. Zeng L. Microfracturing in the upper Triassic Sichuan basin tight-gas sandstones: tectonic, overpressure, and diagenetic origins. *AAPG Bull*. 2010;94(12):1811-1825.

4. Connolly P, Cosgrove J. Prediction of fracture-induced permeability and fluid flow in the crust using experimental stress data. *AAPG Bull*. 1999;83:757-777.

5. Dai J, Feng J, Li M. Discussion on the extension law of structural fracture in sand-mud interbed formation. *Earth Sci Front*. 2011;18:277-283.

6. Gale JFW, Laubach SE, Olson JE, Eichhuble P, Fall A. Natural fractures in shale: a review and new observations. *AAPG Bull*. 2014;98(11):2165-2216.

7. Liu J, Ding W, Wang R, Yin S, Yang H, Gu Y. Simulation of paleotectonic stress fields and quantitative prediction of multi-period fractures in shale reservoirs: a case study of the Niutitang formation in the lower Cambrian in the Cen'gong block, South China. *Mar Pet Geol*. 2017;84:289-310.

8. Nelson RA. *Geologic Analysis of Naturally Fractured Reservoirs*. Houston, TX: Gulf Publishing; 1985.

9. Pireh A, Alavi SA, Ghassemi MR, Shaban A. Analysis of natural fractures and effect of deformation intensity on fracture density in Garau formation for shale gas development within two anticlines of zagros fold and thrust belt, Iran. *J Pet Sci Eng*. 2015;125:162-180.

10. Lai J, Li D, Wang G, et al. Earth stress and reservoir quality evaluation in high and steep structure: the Lower Cretaceous in the Kuqa Depression, Tarim Basin, China. *Mar Pet Geol*. 2019;101:43-54.

11. Liu J, Ding W, Xiao Z, Dai J. Advances in comprehensive characterization and prediction of reservoir fractures. *Prog Geophys*. 2019;34(6):2283-2300 (in Chinese).

12. Zeng L, Gao C, Qi J, Wang Y, Li L, Qu X. The distribution rule and seepage effect of the fractures in the ultra-low permeability sandstone reservoir in East Gansu Province, Ordos Basin. *Sci China Ser D Earth Sci*. 2008;51(S2):44-52.

13. Zeng L, Li X-Y. Fractures in sandstone reservoirs with ultra-low permeability: a case study of the upper Triassic Yanchang formation in the Ordos basin, China. *AAPG Bull*. 2009;93(4):461-477.

14. Jiang L, Qiu Z, Wang Q, et al. Joint development and tectonic stress field evolution in the Southeastern Mesozoic Ordos basin, west part of North China. *J Asian Earth Sci*. 2016;127:47-62.

15. Jiu K, Ding W, Huang W, You S, Zhang Y, Zeng W. Simulation of paleotectonic stress fields within paleogene shale reservoirs and prediction of favorable zones for fracture development within the Zhanhua depression, Bohai bay basin, East China. *J Pet Sci Eng*. 2013;110:119-131.

16. Ju W, Hou G, Feng S, et al. Quantitative prediction of the Yanchang formation Chang 63 reservoir tectonic fracture in the Qingcheng-Heshui area, Ordos basin. *Earth Sci Front*. 2014;21(6):310-320.

17. Wu Z, Zuo Y, Wang S, et al. Numerical study of multi-period palaeotectonic stress fields in lower Cambrian shale reservoirs and the prediction of fractures distribution: a case study of the Niutitang formation in Feng'gang No. 3 block, South China. *Mar Pet Geol*. 2017;80:369-381.

18. Zhao W-T, Hou G-T. Fracture prediction in the tight-oil reservoirs of the Triassic Yanchang formation in the Ordos basin, Northern China. *Pet Sci*. 2017;14(1):1-23.

19. Beekman F, Badsi M, van Wees J-D. Faulting, fracturing and *in situ* stress prediction in the Ahnet basin, Algeria—a finite element approach. *Tectonophysics*. 2000;320(3-4):311-329.

20. Guo P, Yao L, Ren D. Simulation of three-dimensional tectonic stress fields and quantitative prediction of tectonic fracture within the Damintun depression, Liaohe basin, Northeast China. *J Struct Geol*. 2016;86:211-223.

21. Liu J, Ding W, Yang H, et al. 3D geomechanical modeling and numerical simulation of *in-situ* stress fields in shale reservoirs: a case study of the lower Cambrian Niutitang formation in the Cen'gong block, South China. *Tectonophysics*. 2017;712-713:663-683.

22. Liu J, Ding W, Dai J, Wu Z, Yang H. Quantitative prediction of lower order faults based on the finite element method: a case study of the M35 fault block in the western Hanliu fault zone in the Gaoyou sag, East China. *Tectonics*. 2018;37(10):3479-3499.

23. Paul S, Chatterjee R. Determination of *in-situ* stress direction from cleat orientation mapping for coal bed methane exploration in south-eastern part of Jharia coalfield, India. *Int J Coal Geol*. 2011;87(2):87-96.

24. Zang PDA, Stephansson O. *Stress Field of the Earth's Crust*. Netherlands: Springer; 2010.

25. Ameen MS. Fracture and *in-situ* stress characterization of hydrocarbon reservoirs: definitions and introduction. *Geol Soc Lond Spec Publ*. 2003;209(1):1-6.

26. Burra A, Esterle JS, Golding SD. Horizontal stress anisotropy and effective stress as regulator of coal seam gas zonation in the Sydney basin, Australia. *Int J Coal Geol*. 2014;132:103-116.

27. Nie X, Zou C, Pan L, Huang Z, Liu D. Fracture analysis and determination of *in-situ* stress direction from resistivity and acoustic image logs and core data in the Wenchuan earthquake fault scientific drilling borehole-2 (50–1370m). *Tectonophysics*. 2013;593:161-171.

28. Rajabi M, Sherkati S, Bohloli B, Tingay M. Subsurface fracture analysis and determination of *in-situ* stress direction using FMI logs: an example from the Santonian carbonates (Ilam formation) in the Abadan Plain, Iran. *Tectonophysics*. 2010;492(1-4):192-200.

29. Snow DT. Anisotropie permeability of fractured media. *Water Resour Res*. 1969;5(6):1273-1289.

30. Oda M. Permeability tensor for discontinuous rock masses. *Géotechnique*. 1985;35(4):483-495.

31. Renard P, Genty A, Stauffer F. Laboratory determination of the full permeability tensor. *J Geophys Res Solid Earth*. 2001;106(B11):26443-26452.

32. Min K-B, Rutqvist J, Tsang C-F, Jing L. Stress-dependent permeability of fractured rock masses: a numerical study. *Int J Rock Mech Min Sci*. 2004;41(7):1191-1210.

33. Wong RCK, Du J. Application of strain-induced permeability model in a coupled geomechanics-reservoir simulator. In: *Canadian International Petroleum Conference*. Calgary, Alberta: Petroleum Society of Canada; 2003:1-14.

34. Wong RCK, Li Y. A deformation-dependent model for permeability changes in oil sand due to shear dilation. *J Can Pet Technol*. 2001;40(08):37-44.

35. Bagheri M, Settari A. Methods for modelling full tensor permeability in reservoir simulators. *J Can Pet Technol*. 2007;46:31-38.

36. Hassanpour RM, Manchuk JG, Leuangthong O, Deutsch CV. Calculation of permeability tensors for unstructured gridblocks. *J Can Pet Technol*. 2010;49(10):65-74.

37. Dayani S, Baghbanan A, Karami M. Evaluating the permeability tensor of a fractured rock mass using effective medium theory. In: *ISRM International Symposium - EUROCK 2012*. Stockholm, Sweden: International Society for Rock Mechanics and Rock Engineering; 2012:1-12.

38. Metwally Y, Chesnokov EM. Measuring gas shale permeability tensor in the lab scale. In: *2010 SEG Annual Meeting*. Denver, CO: Society of Exploration Geophysicists; 2010:1-6.

39. Rong G, Peng J, Wang X, Liu G, Hou D. Permeability tensor and representative elementary volume of fractured rock masses. *Hydrogeol J*. 2013;21(7):1655-1671.

40. Chen D, Pan Z, Ye Z. Dependence of gas shale fracture permeability on effective stress and reservoir pressure: model match and insights. *Fuel*. 2015;139:383-392.

41. Pereira GG. Fluid flow, relative permeabilities and capillary pressure curves through heterogeneous porous media. *Appl Math Model*. 2019;75:481-493.

42. Cui Y, Wang G, Jones SJ, et al. Prediction of diagenetic facies using well logs – a case study from the upper Triassic Yanchang formation, Ordos basin, China. *Mar Pet Geol*. 2017;81:50-65.

43. Xu Z, Liu L, Wang T, et al. Characteristics and controlling factors of lacustrine tight oil reservoirs of the Triassic Yanchang formation Chang 7 in the Ordos basin, China. *Mar Pet Geol*. 2017;82:265-296.

44. Zhang W, Yang W, Xie L. Controls on organic matter accumulation in the Triassic Chang 7 lacustrine shale of the Ordos basin, Central China. *Int J Coal Geol*. 2017;183:38-51.

45. Willis-Richards J, Watanabe K, Takahashi H. Progress toward a stochastic rock mechanics model of engineered geothermal systems. *J Geophys Res Solid Earth*. 1996;101(B8):17481-17496.

46. Hicks TW, Pine RJ, Willis-Richards J, Xu S, Jupe AJ, Rodrigues NEV. A hydro-thermo-mechanical numerical model for HDR geothermal reservoir evaluation. *Int J Rock Mech Min Sci Geomech Abstr*. 1996;33(5):499-511.

47. Durham WB, Bonner BP. Self-propping and fluid flow in slightly offset joints at high effective pressures. *J Geophys Res Solid Earth*. 1994;99(B5):9391-9399.

48. Qin JS. Variation of the permeability of the low-permeability sandstone reservoir under variable confined pressure. *J Xian Pet Inst*. 2002;17:28-31.

49. Rajabi M, Tingay M, King R, Heidbach O. Present-day stress orientation in the Clarence-Moreton basin of New South Wales, Australia: a new high density dataset reveals local stress rotations. *Basin Res*. 2017;29:622-640.

50. Tingay MRP, Morley CK, Hillis RR, Meyer J. Present-day stress orientation in Thailand's basins. *J Struct Geol*. 2010;32(2):235-248.

51. Zeng L, Tang X, Jiang J, Peng Y, Yang Y, Lyu W. Unreliable determination of *in situ* stress orientation by borehole breakouts in fractured tight reservoirs: a case study of the upper Eocene Hetaoyuan formation in the Anpeng Field, Nanxiang basin, China. *AAPG Bull*. 2015;99(11):1991-2003.

52. Zoback MD. *Reservoir Geomechanics*. Cambridge, UK: Cambridge University Press; 2007.

53. Li M, Qin S, Ma P, Sun Q. In-situ stress measurement with Kaiser effect of rock acoustic emission. *J Eng Geol*. 2008;16(6):833-838.

54. Lavrov A. The Kaiser effect in rocks: principles and stress estimation techniques. *Int J Rock Mech Min Sci*. 2003;40(2):151-171.

55. Lin Y, Ge H, Wang S. Testing study on dynamic and static elastic parameters of rocks. *Chin J Rock Mech Eng*. 1998;17(2):216-222.

56. Lu B. Advances in calculation methods for rock mechanics parameters. *Pet Drill Techn*. 2005;33(5):44-47.

57. Zhao W, Hou G, Hari KR. Two episodes of structural fractures and their stress field modeling in the Ordos block, Northern China. *J Geodyn*. 2016;97:7-21.

APPENDIX 1

$$a = \sin\delta\,\sin\omega$$

$$b = \sin\delta\,\cos\omega$$

$$c = \cos\delta$$

$$e = \sin\alpha\,\sin\beta$$

$$f = \sin\alpha\,\cos\beta$$

$$g = \cos\alpha$$

$$m_{11} = ae + bf + cg$$

$$m_{12} = \frac{be - af}{\sin\delta}$$

$$m_{13} = \frac{-ace - bcf + g\sin^2\delta}{\sin\delta}$$

$$m_{21} = \frac{af\cos\theta - aeg\sin\theta - bfg\sin\theta - be\cos\theta + c\sin^2\alpha\,\sin\theta}{\sin\alpha}$$

$$m_{22} = \frac{bf\cos\theta - beg\sin\theta + afg\sin\theta + ae\cos\theta}{\sin\delta\,\sin\alpha}$$

$$m_{23} = \frac{-acf\cos\theta + aceg\sin\theta + befg\sin\theta + bce\cos\theta + \sin^2\delta\,\sin^2\alpha\,\sin\theta}{\sin\delta\,\sin\alpha}$$

$$m_{31} = \frac{-af\sin\theta - aeg\cos\theta + be\sin\theta - bfg\cos\theta + c\sin^2\alpha\,\cos\theta}{\sin\alpha}$$

$$m_{32} = \frac{-bf\sin\theta - beg\cos\theta - ae\sin\theta + afg\cos\theta}{\sin\delta\,\sin\alpha}$$

$$m_{33} = \frac{acf\sin\theta + aceg\cos\theta - bce\sin\theta + bcfg\cos\theta + \sin^2\delta\,\sin^2\alpha\,\cos\theta}{\sin\delta\,\sin\alpha}$$